CFD-DEM simulation of three-dimensional aeolian sand movement

YANG JieCheng, ZHANG Yu[*], LIU DaYou & WEI XiaoLin

Key Laboratory of Environmental Mechanics, Institute of Mechanics, Chinese Academy of Sciences, Beijing 100190, China

A three-dimensional CFD-DEM model is proposed to investigate the aeolian sand movement. The results show that the mean particle horizontal velocity can be expressed by a power function of heights. The probability distribution of the impact and lift-off velocities of particles can be described by a log-normal function, and that of the impact and lift-off angles can be expressed by an exponential function. The probability distribution of particle horizontal velocity at different heights can be described as a lognormal function, while the probability distribution of longitudinal and vertical velocity can be described as a normal function. The comparison with previous two-dimensional calculations shows that the variations of mean particle horizontal velocity along the heights in two-dimensional and three-dimensional models are similar. However, the mean particle density of the two-dimensional model is larger than that in reality, which will result in the overestimation of sand transportation rate in the two-dimensional calculation. The study also shows that the predicted probability distributions of particle velocities are in good agreement with the experimental results.

Research studies have increasingly focused on the aeolian sand movement, for it is responsible for a series of serious environmental problems, such as desertification and sand storms. The movement of particles can be divided into creep, saltation and suspension, and saltation is the most important type of movement, accounting for about three fourths of the total sand flux [1]. Therefore, saltation is the key point of the research on the aeolian sand movement. The model created in this paper mainly simulates the aeolian sand movement in the region near the surface of the sand bed, including creep and saltation. The distributions of particle velocities in this region are used to reflect the creep and saltation motion state.

The collision and lift-off of particles are very important in the region near the surface of the sand bed. Particles transfer air momentum to the sand bed surface and splash more particles into the air by the collisions with the surface of sand bed. The collision processes determine not only the distribution of particle lift-off velocities, but also the status of the whole aeolian sand field [2]. Therefore, this paper also focuses on the probability distributions of particle impact velocity, impact angle, lift-off velocity and lift-off angle.

Field observations, wind tunnel experiments, numerical simulations and theoretical analysis are the main approaches taken by the researchers to the aeolian sand movement. With the set up of the Aeolian sand physics by Bagnold, remarkable progress has been made in wind tunnel experiments and field observations. Zou [3] used high-speed photography methods to study particle saltation movement in the wind tunnel, and the results showed that the distribution of particle velocity along the height followed the power function pattern. Dong [4] measured the sand flux above the sand bed surface with a sand trapper, and his results showed

*Corresponding author (email: zhangyu@imech.ac.cn)

that the exponential function can describe the variation of sand flux with height. Kang [5] got the probability distributions of particle impact and lift-off velocities on bed surface and the particle velocity distributions at different heights in a wind tunnel with the PDPA (Phase Doppler Particle Analyzer) measurement technology. The results showed that the probability distribution of impact and lift-off velocities of sand grains can be expressed by a log-normal function, and that of impact and lift-off angles complies with an exponential function. Kang also suggested describing the probability distribution of particle vertical velocity with a normal function.

At the same time, an increasing number of scholars simulate the aeolian sand movement through some mathematical models. In recent models, the aeolian sand movement is generally divided into four different processes, such as aerodynamic entrainment, grain trajectories, grain-bed impacts, and wind field modification. In the model created by Ungar [6] and McEwan [7], collisions between particles and sand bed are described by a splash function. However, the research of Anderson [8] showed that the number of grains due to aerodynamic entrainment is rare at a steady state, and particle impacts mainly cause the saltating grains to jump from sand bed into air. Huang [9] created a model which considered the effect of mid-air collisions of particles, and found that the mass flux at heights and the sand transport rate are much closer to the corresponding experimental values than those results when the mid-air collision is not considered. Hence, it is important to study the collisions between the particles and sand bed, but mid-air collisions of particles should not be neglected. The model in this paper considers the two kinds of collisions.

The Aeolian sand movement is a complex gas-solid two-phase flow and the momentum exchange between air and particles is also complicated. The results of field observations showed that the wind profile followed a logarithmical function in the near-bed layer before the aeolian sand movement started. However, after the movement occurred, the wind profile was modified due to the drag of particles. For that reason, a model that considers the coupling effect between the two phases better fits the aeolian sand movement simulation. Huang [10] developed a model in which a set of experimentally determined nonlogarithmic wind profiles are employed and found that the trajectory heights and lengths of particles obtained by nonlogarithmic wind profiles are very different from those calculated by the logarithmically distributed profiles. Huang [11] also created a numerical model which took into consideration the effect of thermal flux from the surface to the atmospheric boundary layer to simulate the fine structure and development of a dust devil, and indicated that the formation mechanisms of a dust devil could be explained with the theory of thermal convection. Zheng [12] set up a model which considered the drag force between fluid and particles, gravitational force

and electrostatic force to simulate the aeolian sand movement and reported that all three forces affected the movement. Kang [13] created a two-dimensional model which treats particles as plates with an identical diameter, introduced the soft sphere model for particle-bed and particle-particle collisions and considered the coupling interaction between the saltation particles and air, and got the distributions of particle velocity and sand flux. However, the statistical sand flux results are still in need of further improvement because the simulation is only two-dimensional.

A three-dimensional CFD-DEM model, which applies the soft sphere model for inter-particle collisions with the coupling effect between the gas phase and solid phase taken into consideration, is created in this paper to simulate the aeolian sand movement in the region near the surface of sand bed. The distribution of mean particle horizontal velocity, the probability distributions of particle impact velocity and angle and particle lift-off velocity and angle, and the probability distributions of particle horizontal, longitudinal and vertical velocity at different heights and their fixed fit expressions are got from the simulation.

1   Mathematical model

1.1   Equations of gas phase

The continuity and momentum equations of the gas phase are as follows:

$$\frac{\partial}{\partial t}(\alpha_f \rho_f) + \nabla \cdot (\alpha_f \rho_f \boldsymbol{u}_f) = 0, \tag{1}$$

$$\frac{\partial}{\partial t}(\alpha_f \rho_f \boldsymbol{u}_f) + \nabla \cdot (\alpha_f \rho_f \boldsymbol{u}_f \boldsymbol{u}_f)$$
$$= -\alpha_f \nabla p + \nabla \cdot (\alpha_f \boldsymbol{\tau}_f) + \alpha_f \rho_f g - \boldsymbol{f}_{\text{drag}}, \tag{2}$$

where subscript f indicates the gas phase, ρ_f, $\boldsymbol{u}_f$ and p are the fluid density, velocity and pressure, respectively. g is gravity acceleration. $\boldsymbol{\tau}_f$ is the fluid shear stress. α_f is the volume fraction of fluid, and $\boldsymbol{f}_{\text{drag}}$ is the volumetric fluid-particle interaction force. $\boldsymbol{\tau}_f$, α_f and $\boldsymbol{f}_{\text{drag}}$ are expressed as follows:

$$\boldsymbol{\tau}_f = -\frac{2}{3}(\mu_{\text{eff}}\nabla \cdot \boldsymbol{u}_f)\mathbf{I} + \mu_{\text{eff}}[\nabla \boldsymbol{u}_f + (\nabla \boldsymbol{u}_f)^{\text{T}}], \tag{3}$$

$$\alpha_f = 1 - \sum_{k=1}^{n_p} V_{pk} / \Delta V, \tag{4}$$

$$\boldsymbol{f}_{\text{drag}} = \frac{1}{\Delta V}\sum_{i=1}^{n_p} \boldsymbol{F}_{\text{drag},i}, \tag{5}$$

where μ_{eff} is the fluid effective viscosity, I is unit tensor, ΔV and V_{pk} are the volume of a computational cell and the

volume of particle k inside this cell, respectively, and n_p is the number of particles in the cell. For the three-dimensional flow, $\Delta V = \Delta x \Delta y \Delta z$, Δx, Δy and Δz are the lengths of a computational cell in the x, y and z directions, respectively.

$F_{\text{drag},i}$ is the fluid drag force on particle i, which can be described by Di Felice [14] as:

$$F_{\text{drag},i} = \frac{C_{d0}}{8} \pi d_p^2 \rho_f \alpha_f^2 |u_f - u_p|(u_f - u_p)\alpha_f^{-\chi}, \tag{6}$$

where $\chi = 3.7 - 0.65 \exp[-(1.5 - \log Re_p)^2 / 2]$, C_{d0} and Re_p are the fluid drag coefficient and the particle Reynolds number, respectively:

$$C_{d0} = \left(0.63 + \frac{4.8}{Re_p^{0.5}}\right)^2, \tag{7}$$

$$Re_p = \frac{\alpha_f \rho_f d_p |u_f - u_p|}{\mu_f}. \tag{8}$$

As the air in the aeolian sand movement is in a turbulent state, the effect of fluid turbulence should be considered. The fluid turbulence can be treated with the standard k-ε turbulent model as follows:

$$\frac{\partial}{\partial t}(\alpha_f \rho_f k) + \nabla \cdot (\alpha_f \rho_f u_f k)$$
$$= \nabla \cdot (\alpha_f \Gamma_k \nabla k) + \alpha_f G - \alpha_f \rho_f \varepsilon + S_k, \tag{9}$$

$$\frac{\partial}{\partial t}(\alpha_f \rho_f \varepsilon) + \nabla \cdot (\alpha_f \rho_f u_f \varepsilon)$$
$$= \nabla \cdot (\alpha_f \Gamma_\varepsilon \nabla \varepsilon) + \alpha_f \frac{\varepsilon}{k}(c_1 G - c_2 \rho_f \varepsilon) + S_\varepsilon, \tag{10}$$

where $G = \mu_{ft} \nabla u_f \cdot [\nabla u_f + (\nabla u_f)^T]$, $\Gamma_k = \mu_f + \dfrac{\mu_{ft}}{\sigma_k}$, $\Gamma_\varepsilon = \mu_f + \dfrac{\mu_{ft}}{\sigma_\varepsilon}$. μ_f is the fluid dynamic viscosity and μ_{ft} is the turbulent viscosity. $\mu_{ft} = c_\mu \rho_f k^2 / \varepsilon$, $\mu_{\text{eff}} = \mu_f + \mu_{ft}$. c_1, c_2 and c_μ are constants, $c_1 = 1.44$, $c_2 = 1.92$ and $c_\mu = 0.09$. S_k and S_ε are the source terms of the gas turbulence kinetic energy and its dissipation rate induced by particles. However, those terms have not yet been considered in the current simulation, and will be considered in further research.

1.2   Equations of particle motion

The equations of particle translational and rotational motion are expressed by

$$m_p \frac{d u_{p,l}}{dt} = m_p g + F_{\text{drag},l} + \sum_{k=1}^{n_c}(f_{n,lk} + f_{t,lk}), \tag{11}$$

$$I_p \frac{d \omega_l}{dt} = \sum_{k=1}^{n_c} T_{lk}, \tag{12}$$

where m_p, $u_{p,l}$ and ω are the mass, translational and angular velocity of particle l, respectively. $f_{n,lk}$, $f_{t,lk}$ and T_{lk} are the normal collision force, tangential collision force and torque between particles l and k, respectively. $T_{lk} = R_l \times (f_{n,lk} + f_{t,lk})$. R_l is the vector from the center of particle l to the collision point. I_p is the moment of inertia of the particle, $I_p = \frac{1}{10} m_p d_p^2$. n_c is the number of the particles in contact with particle l.

1.3   Inter-particle collision model

The soft sphere model is used to describe inter-particle collisions as it is suitable for treating the multiple particle collisions. According to the linear spring model [15], the normal and tangential inter-particle forces can be described as follows:

$$f_{n,lk} = -k_s \delta_n - \eta v_{n,lk}, \tag{13}$$

$$f_{t,lk} = \begin{cases} -k_s \delta_t - \eta v_{t,lk}, & |f_{t,lk}| \leqslant \mu_s |f_{n,lk}|, \\ -\mu_s |f_{n,lk}| t, & |f_{t,lk}| > \mu_s |f_{n,lk}|, \end{cases} \tag{14}$$

where subscripts n and t indicate the normal and tangential directions. k_s and η are the stiffness and damping coefficients, respectively. μ_s is the friction coefficient. δ is the displacement vector between two contacting particles, and v is the relative velocity vector between two contacting particles, $v_{n,lk} = (v_{lk} \cdot n)n$, $v_{t,lk} = v_{lk} - v_{n,lk}$, $v_{lk} = v_l - v_k + \omega_l \times R_l - \omega_k \times R_k$. n is the unit vector from the centre of particle l to that of particle k, $n = R_l / |R_l|$. t is the unit tangential vector, $t = v_{t,lk} / |v_{t,lk}|$.

2   Simulated conditions

The computational domain is a 0.03 m-long, 0.002 m-wide and 0.3 m-high three-dimensional cubic region as shown in Figure 1. The periodic boundary condition is used for both the front-back and left-right boundaries. For gas, the gas velocity of the outlet is given to the inlet. For particles, when a particle leaves from the inlet or the outlet, it will enter the domain via the other. On the top boundary, the constant shear stress τ_0 is set for the gas (τ_0 is different in different cases, and the corresponding friction velocity u_* is

defined as $u_* = \sqrt{\tau_0 / \rho_{\mathrm{f}}}$), and the reflective boundary condition is used for particles, which means that if a particle leaves the top boundary at the velocity of (u_p, v_p, w_p), another particle will enter the boundary at the velocity of $(u_p, v_p, -w_p)$. On the bottom boundary, the non-slip condition is used for gas. The particle-wall collision is treated in the same manner as a particle-particle collision, and the wall is considered one particle with an infinitely large radius, an infinitely large mass and a zero velocity vector.

When the fluid field driven by the constant shear stress of air on the top boundary is static, N particles are generated randomly in the region 50 mm high from the bottom boundary of the computational domain (N is the number of the particles, and N is different in different cases). Because of the results of a stable state as our concern, the initial state of simulation can be inconsistent with the actual condition, but the initial state must be able to converge to a stable state. The sand bed in true aeolian sand movement is very thick, but not all the layers can move. In a few layers below, the sand particles are almost static. Therefore, we set the bottom boundary as a stationary plate (equivalent to a static particle with an infinitely large radius), and use it to replace all the particles below it. For the movement of many particles above, this substitution is in general equivalent, but it will cause some error. The more sand layers we choose, the smaller the difference between the actual situation and the condition we set is. However, the more sand layers we choose, the much more time the simulation will take. Out of a comprehensive consideration of the two factors above, we chose a compromised number of particles, which is the number when particles accumulated 12 layers in the vertical direction. These particles are generated in the region 50 mm high from the bottom boundary when $t = 0$, and their initial positions are random and their initial velocities are all 0. Setting initial conditions as described above can make particles collide with each other when they drop to form the sand bed, which is helpful to start the aeolian sand movement. When the total sand mass flux in the computational region does not change any more (random fluctuations will exit), it indicates that the aeolian sand movement has reached a static state.

The fluid field shaped by the transmission of the constant shear stress can save computational time if particles are generated after the fluid field is static. Moreover, generating particles randomly in the region 50 mm high from the bottom boundary can make particles collide with each other

when they drop to form the sand bed, which is helpful to start the aeolian sand movement and reach the static status.

The particles diameters in each case are identical (particle diameter d_{p} is different in different cases). The particle density is 2650 kg/m^3. The stiffness coefficient is 1500 N/m, the damping coefficient is 0.002 N s/m, and the friction coefficient is 0.4. The computational time-step for particles is chosen as 2.0×10^{-6} s, and the time-step for fluid is 2.0×10^{-5} s. Haff [16] noted that the precise value of friction coefficient had little overall effect on the impact event when the friction coefficient is between 0.25 and 2.0. Yuu [17] found that in the order of 1000 N/m, the value of stiffness had little effect on the particle behaviour. Hence, the friction coefficient is 0.4, the stiffness coefficient is 1500 N/m, and the damping coefficient is 0.002 N s/m in this paper. The particles are softer in order to get a larger time-step and fewer iterations. As the particle diameter is bigger, a larger friction velocity is chosen than that in real aeolian sand movement so as to drive more particles. All these methods are used for reducing the computational time and getting the converged results faster.

Results of the three cases are got in this paper (Case 1, Case 2 and Case 3). The differences of simulated conditions of the three cases are shown in Table 1, and the other conditions remain the same as described above.

3   Results and discussion

3.1   Variation of mean particle horizontal velocity with height
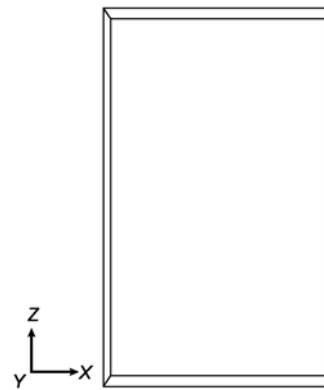
The variation of mean particle horizontal velocity with

Figure 1   The sketch of the computational domain.

Table 1   The description of simulation cases

Serial number	Simulated particle numbers N	Particle diameter d_{p} (m)	The shear stress of top boundary τ_0 (Pa)
Case 1	6480	0.00033	14.7
Case 2	17000	0.00020	14.7
Case3	17000	0.00020	7.5

height is important in studying the kinetic energy distribution, which determines the variation of erosion intensity with height [18]. Therefore, the sand velocity is a key parameter in the study of aeolian sand movement.

Results of the variation of mean particle horizontal velocity with heights of three cases are shown in Figure 2. It can be seen that the mean particle horizontal velocity increases with height, and the variation of the non-dimensional mean particle horizontal velocity with height can be described by a power function as follows:

$$\frac{u_{\mathrm{p}}}{u_*} = A \cdot \left(\frac{h}{d_{\mathrm{p}}} \right)^B , \tag{15}$$

where u_{p} is the mean particle horizontal velocity (m/s), u_* is the friction velocity (m/s), h is the height (m), d_{p} is the particle diameter (m), and A and B are the fitting parameters.

Table 2 lists the fitting parameters of the mean particle horizontal velocity distribution. R^2 is the correlation coefficient. It can be seen that the correlation coefficients of the three cases are more than 0.97, which means the power function can reasonably describe the mean particle horizontal velocity distribution. Dong [4] and Zou [5] have also found that the horizontal velocity distribution of particles can be expressed by a power function from their experimental observations.

The effect of particle diameter and wind speed on the mean particle horizontal velocity distribution can be seen in Figure 2. Under the condition that particle diameters remain the same, with the increase of the wind speed the particle horizontal velocity also increases. When the wind speed remains the same, smaller particles move faster than bigger

particles. Moreover, the no-dimensional fitting functions for the three cases are in the same form, but parameters of each other are different.

3.2 Comparison of results of two- and three-dimensional models

Figures 3 and 4 show the comparisons of particle velocity and sand mass flux from the three dimensional model in this paper (Case 1), the similar two dimensional model [13] and the similar experiment. d_{p} is the particle diameter in experiments, and u_{f0} is the free-stream wind velocity at mid height of the wind tunnel. It can be seen from Figure 3 that the results of the mean particle horizontal velocity from the two models are basically consistent with the experimental result [19]. However, Figure 4 denotes that the results of sand mass flux from the two-dimensional model are much more than the three-dimensional results and the experimental result [20], while the latter two are almost identical (according to the reference [20], the sand mass flux here is the product of the sand mass transport rate per unit area and the unit height of the sand trap). This is because after particles lift off from the sand bed, they should disperse in the respective x, y and z directions. However, the effect of the
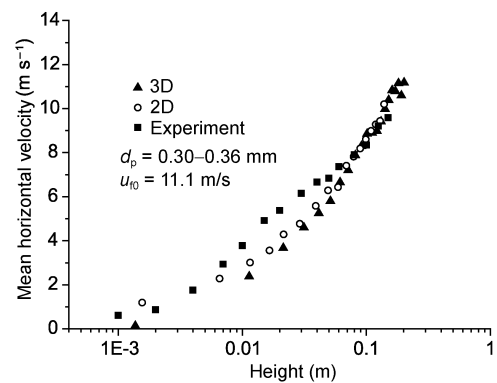
Figure 3   A comparison of the simulated mean horizontal velocity with experimental data.

Table 2   Fitting parameters of the mean particle horizontal velocity

Serial number	A	B	R^2
Case 1	0.10901	0.53367	0.97436
Case 2	5.61003	0.13146	0.99911
Case 3	1.82639	0.23396	0.99048

Figure 2   Variation of the mean particle horizontal velocity with height.
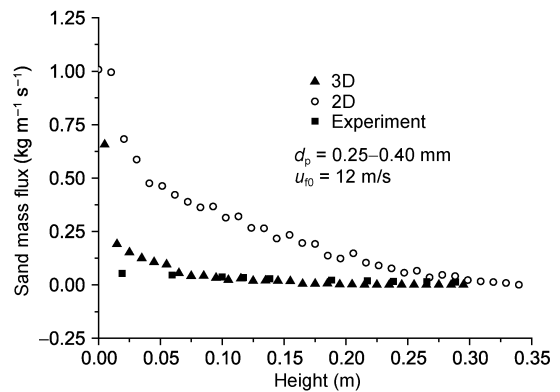
Figure 4   A comparison of the simulated sand mass flux with experimental data.

dispersal in the *y* direction can not be considered in the two-dimensional model. Hence, the mean particle density is magnified unreasonably. This is the most irrational aspect in the two-dimensional model, which results in the obvious overestimation of the sand mass flux. Therefore, the three-dimensional model improves significantly on the two-dimensional model in this aspect.

3.3   Probability distribution of impact velocity and angle of particles near the sand bed surface

In the following results, the impact particles and lift-off particles are defined as: in the region above the sand bed surface 1mm, if the vertical velocity of a particle is downward, it is considered an impact particle, otherwise it is the lift-off particle. Particle impact and lift-off velocities are resultant velocity in the *x*, *y*, *z* directions of impact and lift-off particles, respectively. The particle impact angle is the angle between the particle impact velocity and the horizontal face. The particle lift-off angle is the angle between the particle lift-off velocity and the horizontal face.

The probability distribution of the particle impact velocity is shown in Figure 5. The histogram is the probability from calculation, and the line is the fitting curve. It can be seen from Figure 5 that the probability distributions of the particle impact velocity can be described by a log-normal function as follows:

$$P(u_I) = \frac{A}{\sqrt{2\pi}Bu_I}\exp\left(-\frac{(\ln u_I - \ln C)^2}{2B^2}\right), \qquad (16)$$

where *P* is the probability, u_I is the particle impact velocity (m/s), and *A*, *B* and *C* are the fitting parameters.

Table 3 lists the fitting parameters of the particle impact velocity distribution. R^2 is the correlation coefficient. It can be seen that the correlation coefficients of the three cases are more than 0.96, which means the log-normal function can fairly describe the particle impact velocity distribution. The probability distribution of the particle impact angle is shown in Figure 6. The histogram is the probability from calculation, and the line is the fitting curve. It can be seen from Figure 6 that the probability distributions of the parti-
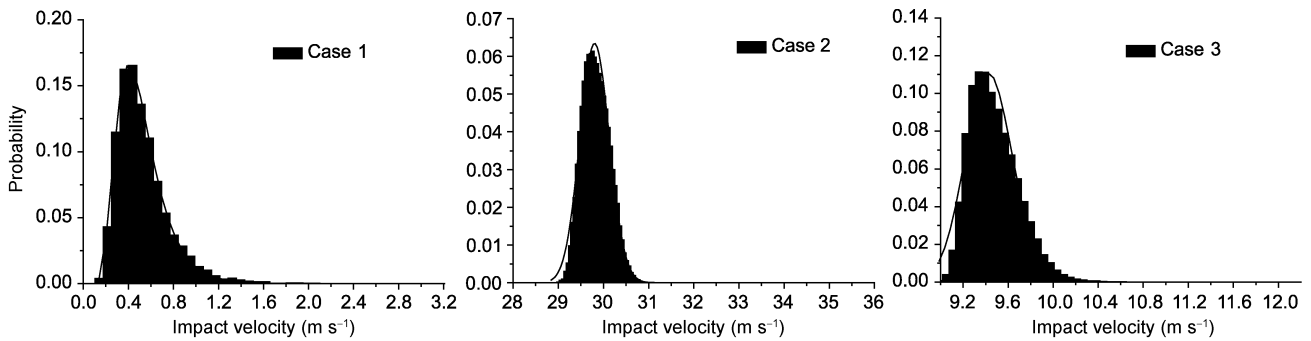

Figure 5   Probability distribution of the particle impact velocity.

Table 3   Fitting parameters of the particle impact velocity distribution

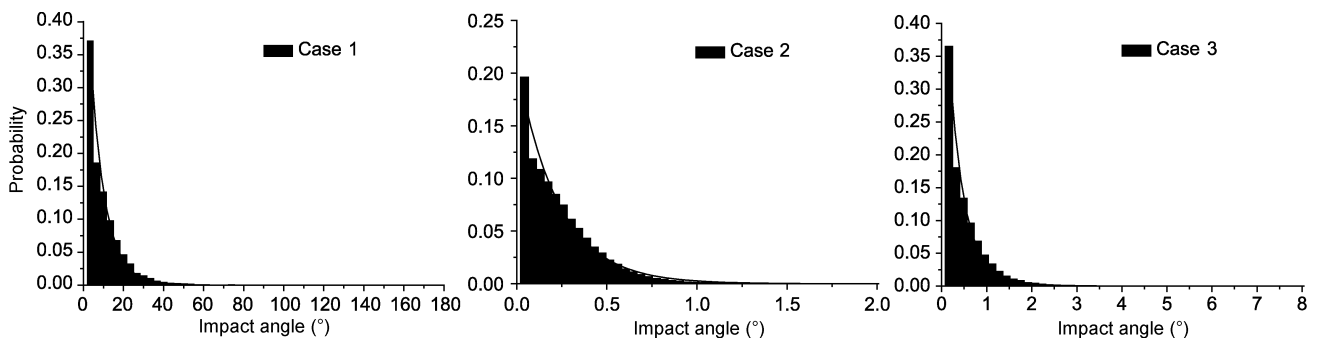| Serial number	*A*	*B*	*C*	R^2
Case 1	0.07266	0.39728	0.4755	0.99876
Case 2	0.0519	0.01095	29.80632	0.98638
Case 3	0.05807	0.02218	9.43039	0.96983

Figure 6   Probability distribution of the particle impact angle.

cle impact angle can be described by an exponential function as follows:

$$P(\alpha_I) = A\exp(-B\alpha_I),\tag{17}$$

where P is the probability, α_I is the particle impact angle (°), and A and B are the fitting parameters.

Table 4 lists the fitting parameters of the particle impact angle distribution. R^2 is the correlation coefficient. It can be seen that the correlation coefficients of the three cases are more than 0.98, which means the exponential function can describe the particle impact angle distribution well.

3.4 Probability distribution of lift-off velocity and angle of particles near the sand bed surface

The probability distribution of the particle lift-off velocity is shown in Figure 7. The histogram is the probability from calculation, and the line is the fitting curve. It can be seen from Figure 7 that the probability distributions of the particle lift-off velocity can be described by a log-normal function as follows:

$$P(u_L) = \frac{A}{\sqrt{2\pi}Bu_L}\exp\left(-\frac{(\ln u_L - \ln C)^2}{2B^2}\right),\tag{18}$$

where P is the probability, u_L is the particle lift-off velocity (m/s), and A, B and C are the fitting parameters.

Table 5 lists the fitting parameters of the particle lift-off velocity distribution. R^2 is the correlation coefficient. It can

be seen that the correlation coefficients of the three cases are more than 0.96, which means the log-normal function can describe the particle lift-off velocity distribution well.

The probability distribution of the particle lift-off angle is shown in Figure 8. The histogram is the probability from calculation, and the line is the fitting curve. It can be seen from Figure 8 that the probability distributions of the particle lift-off angle can be described by an exponential function as follows:

$$P(\alpha_L) = A\exp(-B\alpha_L),\tag{19}$$

where P is the probability, α_L is the particle lift-off angle (°), and A and B are the fitting parameters.

Table 6 lists the fitting parameters of the particle lift-off

Table 4　Fitting parameters of probability distribution of the particle impact angle

Serial number	A	B	R^2
Case 1	0.56145	0.13596	0.98844
Case 2	0.21069	4.37467	0.98115
Case 3	0.54787	2.85421	0.98569

Table 5　Fitting parameters of the particle lift-off velocity distribution

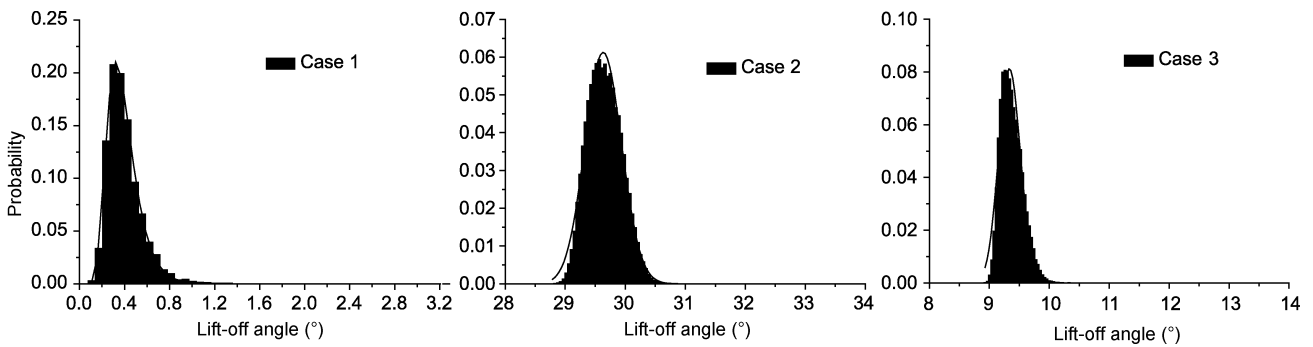| Serial number	A	B	C	R^2
Case 1	0.06333	0.34673	0.3678	0.99871
Case 2	0.04683	0.01029	29.63447	0.98871
Case 3	0.0369	0.01941	9.33828	0.9687

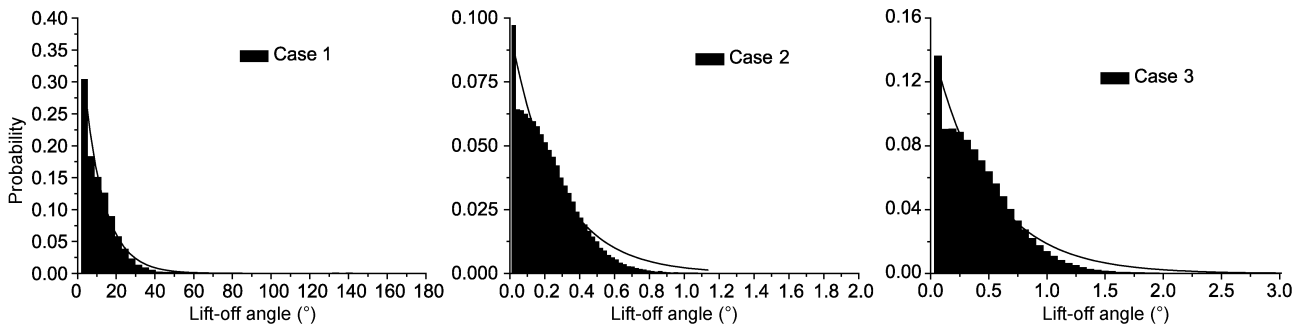**Figure 7**　Probability distribution of the particle lift-off velocity.

Figure 8　Probability distribution of the particle lift-off angle.

Table 6 Fitting parameters of probability distribution of the particle lift-off angle

Serial number	A	B	R^2
Case 1	0.41243	0.09571	0.99
Case 2	0.09553	3.75323	0.95928
Case 3	0.14637	2.05612	0.96901

angle distribution. R^2 is the correlation coefficient. It can be seen that the correlation coefficients of the three cases are more than 0.98, which means the exponential function can describe the particle lift-off angle distribution well.

The comparison of the non-dimensional impact velocity, impact angle, lift-off velocity and lift-off angle between the simulated results from Case1 in this paper and the published experimental results by Kang [5] are shown in Figure 9. The non-dimensional impact velocity is defined as the ratio of the particle impact velocity to its average. The non-dimensional impact angle is defined as the ratio of the particle impact angle to its average. The non-dimensional lift-off velocity is defined as the ratio of the particle lift-off velocity to its average. The non-dimensional lift-off angle is defined as the ratio of the particle lift-off angle to its average. Kang has found that the probability distribution of impact and lift-off velocities of particles can be expressed by a log-normal function, and that of impact and lift-off angles can be expressed by an exponential function. It can be seen from Figure 9 that the simulated probability distribution of the impact and lift-off velocities and the impact and lift-off angles in this paper are accordant with the experimental results.

3.5 Particle velocity distributions at different heights

The particle velocity distribution at different heights is a reflection of the movement of saltation particles [5]. Two heights at the bottom and middle parts, 4 and 20 mm, are selected for analysis. Because the probability of particles reaching higher height is small, and the velocity distribution at a higher height has no much value, no higher height is selected.

The probability of the particle horizontal velocity at different heights is shown in Figure 10. The histogram is the probability from calculation, and the line is the fitting curve. It can be seen that the distributions all have a typical peak and show a positive skewed-ness. The distribution can be expressed by a log-normal function, and this is accordant with the experimental results by Kang [5]. At the 4 mm height, the mean value of the particle horizontal velocity is lower, and the changed range of the particle horizontal velocity is smaller, while at the 20 mm height, the mean value is higher, and the changed range is larger. This is because most particles move in the bottom part of the saltation layer, and only a few particles can reach the higher height by the acceleration of air. So the mean horizontal velocity of these accelerated particles is higher, and the changed range is larger.

The probability of the particle longitudinal velocity at different heights is shown in Figure 11. The histogram is the probability from calculation, and the line is the fitting curve. It can be seen that at the 4 mm height, the distribution is a normal distribution symmetric to zero point. At the 20 mm
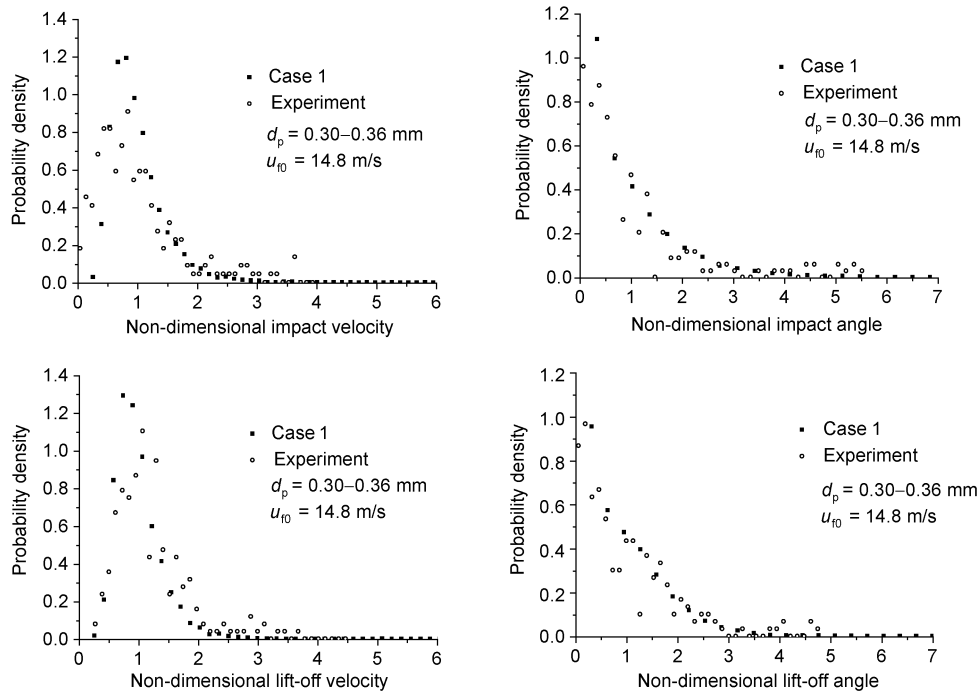

Figure 9 A comparison of the simulated impact and lift-off velocity and angle with experimental data.
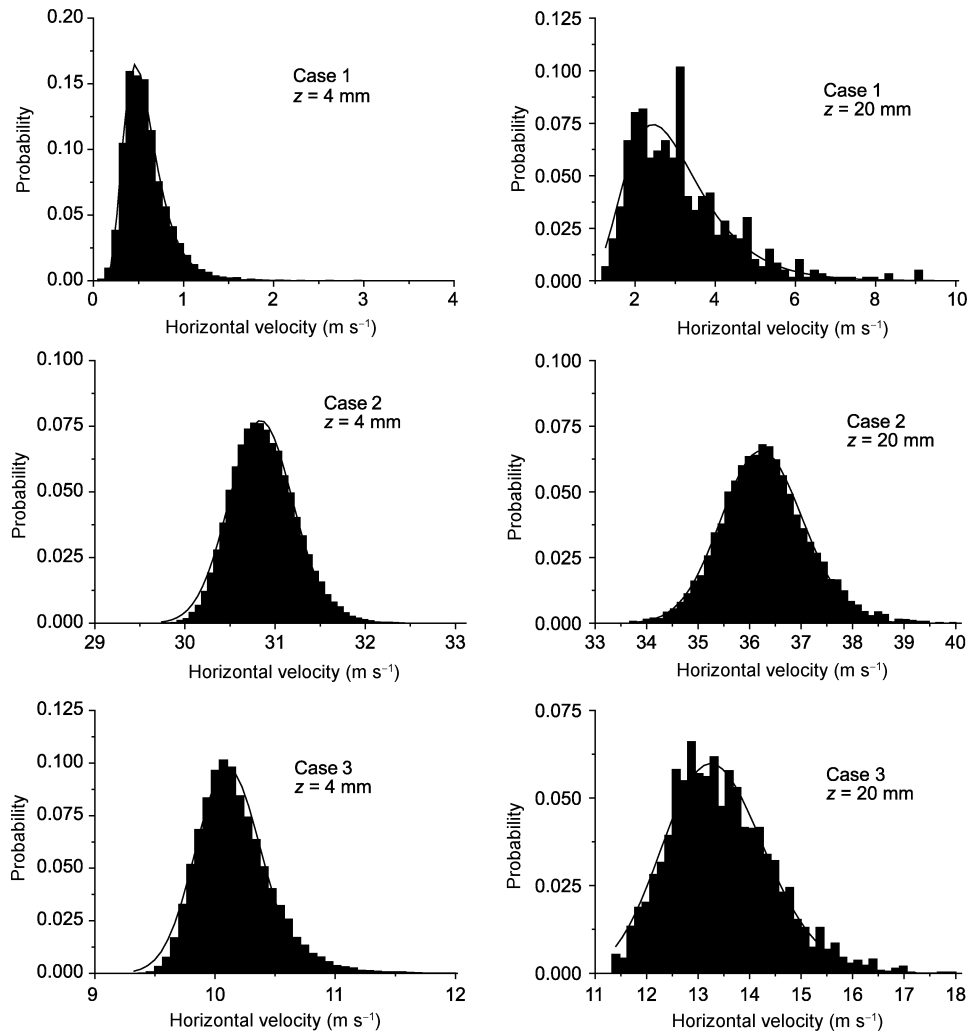
Figure 10   Probability distribution of the particle horizontal velocity.

height, the distribution is similar to a normal distribution symmetric to zero point. This result denotes that the movement of particles in the longitudinal direction is symmetric, which means the probability of particles moving positively equals that of moving negatively. However, the two-dimensional simulation can not give the information in the longitudinal direction.

The probability of the particle vertical velocity at different heights is shown in Figure 12. The histogram is the probability from calculation, and the line is the fitting curve.

It can be seen that the distribution basically accords with a normal distribution symmetric to zero point, with a little leftward skewed-ness. The particle vertical velocity generally changes between −2.5 and 2 m/s, which is consistent with the experimental results of Dong [4] and Kang [5].

Tables 7, 8 and 9 list the fitting parameters of the distributions of particle horizontal velocity, longitudinal velocity and vertical velocity, respectively. The probability distribution of particle horizontal velocity can be described by a log-normal function as follows:

Table 7   Fitting parameters of the particle horizontal velocity distribution

Serial number	Height (mm)	A	B	C	R^2
Case 1	4	0.0775	0.3766	0.53513	0.99679
	20	0.18542	0.37818	2.82232	0.89007
Case 2	4	0.06814	0.01142	30.8439	0.99493
	20	0.12994	0.02179	36.24339	0.99416
Case 3	4	0.06577	0.02652	10.11297	0.98719
	20	0.14733	0.07393	13.31765	0.97205

Table 8   Fitting parameters of the particle longitudinal velocity distribution

Serial number	Height (mm)	A	B	C	R^2
Case 1	4	0.06984	0.25714	−0.00465	0.99089
	20	0.08653	0.84124	0.14271	0.81785
Case 2	4	0.04872	0.40461	−0.00434	0.99957
	20	0.08823	1.07494	−0.01349	0.97875
Case 3	4	0.06255	0.35482	−0.00004	0.99811
	20	0.07706	1.06808	−0.0124	0.9453

Table 9   Fitting parameters of the particle horizontal vertical distribution

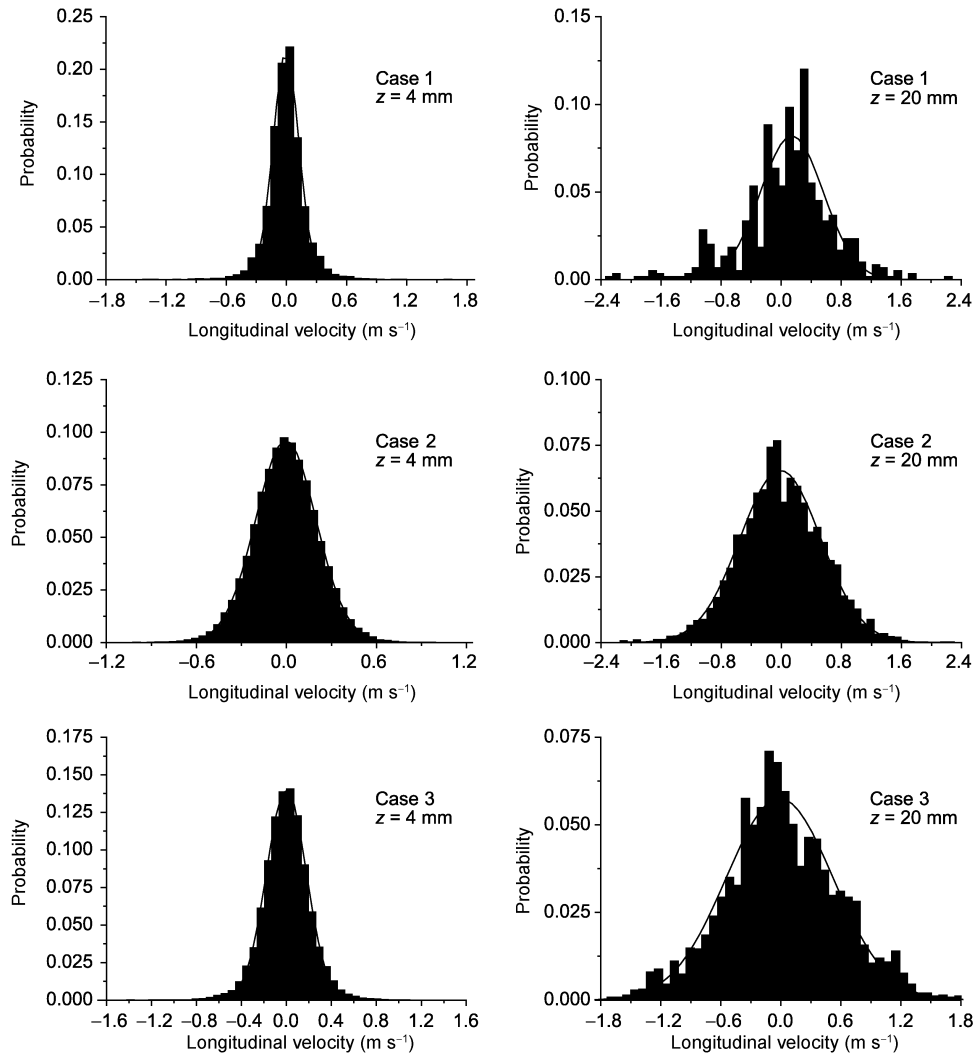| Serial number	Height (mm)	A	B	C	R^2
Case 1	4	0.06865	0.21055	0.0287	0.98738
	20	0.09801	0.95167	0.08782	0.9198
Case 2	4	0.05535	0.37979	0.02092	0.99607
	20	0.07908	0.96267	0.04083	0.98974
Case 3	4	0.06221	0.3097	0.03476	0.98817
	20	0.08449	0.90444	0.06061	0.97823

Figure 11   Probability distribution of the particle longitudinal velocity.
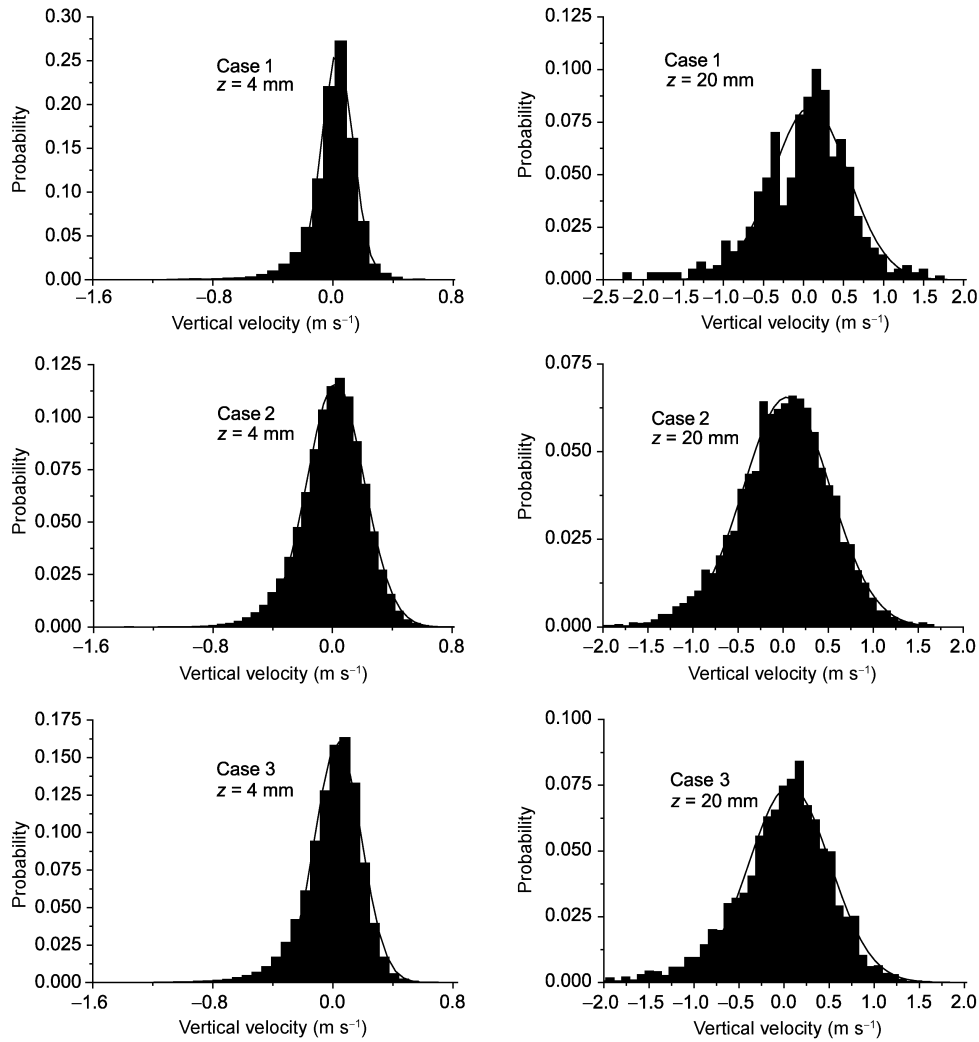
Figure 12   Probability distribution of the particle vertical velocity.

$$P(u_x) = \frac{A}{\sqrt{2\pi}Bu_x}\exp\left(-\frac{(\ln u_x - \ln C)^2}{2B^2}\right), \qquad (20)$$

where P is the probability, u_x is the horizontal velocity (m/s), and A, B and C are the fitting parameters. The probability distribution of particle longitudinal velocity can be described by a normal function as follows:

$$P(u_y) = \frac{A}{\sqrt{\frac{\pi}{2}}B}\exp\left(-\frac{2(u_y - C)^2}{B^2}\right), \qquad (21)$$

where P is the probability, u_y is the longitudinal velocity (m/s), and A, B and C are the fitting parameters. The probability distribution of particle vertical velocity can be described by a normal function as follows:

$$P(u_z) = \frac{A}{\sqrt{\frac{\pi}{2}}B}\exp\left(-\frac{2(u_z - C)^2}{B^2}\right), \qquad (22)$$

where P is the probability, u_z is the longitudinal velocity (m/s), and A, B and C are the fitting parameters. R^2 is the correlation coefficient. It can be seen that all the correlation coefficients of the three cases are more than 0.9, which means the selected functions can describe the particle velocity distributions at different heights well. However, it can be also found that while the distributions of the three cases are similar, there are still different aspects. Further research will focus on analyzing these differences.

The comparison of non-dimensional particle horizontal velocity and particle vertical velocity between the simulated results from Case 1 in this paper and the published experimental results by Kang [5] are shown in Figure 13. The non-dimensional particle horizontal velocity is defined as the ratio of the particle horizontal velocity to its average. The non-dimensional particle vertical velocity is defined as the ratio of the particle vertical velocity to the average of particle horizontal velocity. Kang found that the probability distribution of particle horizontal velocity can be expressed by a log-normal function. It can be seen from Figure 13 that
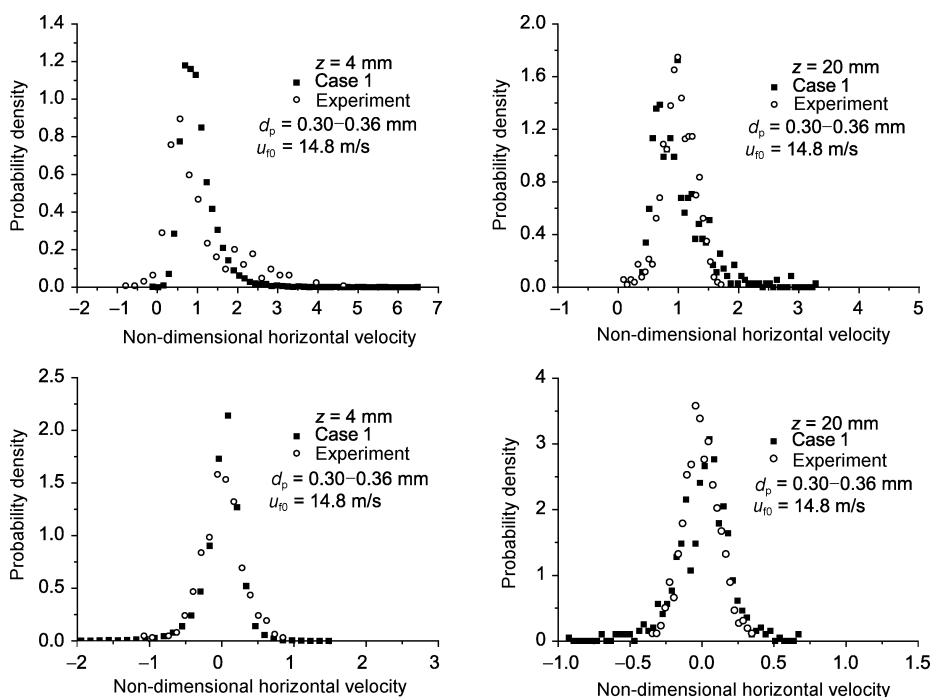
Figure 13 A comparison of the simulated horizontal and vertical velocity with experimental data.

the simulated probability distribution of the particle horizontal velocity and the particle vertical velocity in this paper are generally accordant with the experimental results.

4 Conclusions

The three-dimensional model which applies the soft sphere impact mode for particle impact simulation and which considers the coupling effect between phases can simulate the aeolian sand movement well. Some conclusions are summarized below:

(1) The mean particle horizontal velocity can be expressed by a power function of heights. This is accordant with the published two-dimensional results and experimental results;

(2) The probability distribution of impact and lift-off velocities of particles can be expressed by a log-normal function, and that of impact and lift-off angles can be expressed by an exponential function. This is consistent with the published experimental results;

(3) The probability distribution of particle horizontal velocity at different heights can be described as a lognormal function, while the probability distribution of longitudinal and vertical velocity can be described as a normal function. This is consistent with the published experimental results;

(4) The mean density and sand mass flux from the two-dimensional models which assume particles as plates are larger than experimental results. The three-dimensional model in this paper can correct those errors. As the mean

density and sand mass flux are two key factors in the aeolian sand movement, the three-dimensional model serves the accurate and quantitative study of aeolian sand movement better.

1 Bagnold R A. The Physics of Blown Sand and Desert Dunes. London: Methuen, 1941

2 Cheng H, Zou X Y, Zhang C L. Probability distribution functions for the initial liftoff velocities of saltating sand grains in air. J Geophys Res, 2006, 111: D22205

3 Zou X Y, Wang Z L, Hao Q Z, et al. The distribution of velocity and energy of saltating sand grains in a wind tunnel. Geomorphology, 2001, 36: 155–165

4 Dong Z B, Liu X P, Wang H T, et al. The flux profile of a blowing sand cloud: a wind tunnel investigation. Geomorphology, 2002, 49: 219–230

5 Kang L Q, Guo L J, Liu D Y, Experimental investigation of particle velocity distributions in windblown sand movement. Sci China Ser G-Phys Mech Astron, 2008, 51: 986–1000

6 Ungar J E, Haff P K. Steady state saltation in air. Sedimentology, 1987, 34: 289–299

7 McEwan I K, Willetts B B. Adaptation of the near-surface wind to the development of sand transport. J Fluid Mech, 1993, 252: 99–115

8 Anderson R S, Haff P K. Wind modification and bed response during saltation of sand in air. Acta Mech, 1991, (suppl.1): 21–51

9 Huang N, Ren S, Zheng X J. Effects of the mid-air collision on sand saltation. Sci China Ser G-Phys Mech Astron, 2008, 51: 1416–1426

10 Huang N, Zhang Y L, D'Adamo R. A model of the trajectories and midair collision probabilities of sand particles in a steady state saltation cloud. J Geophys Res, 2007, 112: D08206

11 Huang N, Yue G W, Zheng X J. Numerical simulations of a dust

devil and the electric field in it. J Geophys Res, 2008, 113: D20203

12   Zheng X J, Huang N, Zhou Y. The effect of electrostatic force on the evolution of sand saltation cloud. Eur Phys J E, 2006, 19: 129–138

13   Kang L Q, Guo L J. Eulerian-Lagrangian simulation of aeolian sand transport. Powder Technol, 2006, 162: 111–120

14   Di Felice R. The voidage function for fluid-particle interaction systems. Int J Multiphase Flow, 1994, 20: 153–159

15   Crowe C T, Sommerfeld M, Tsuji Y. Multiphase Flows with Droplets and Particles. Boca Raton: CRC Press, 1998

16   Haff P K, Anderson R S. Grain scale simulations of loose sedimentary beds: The example of grain-bed impacts in aeolian saltation. Sedimentology, 1993, 40: 175–198

17   Yuu S, Abe T, Saitoh T, et al. Three-dimensional numerical simula-

tion of the motion of particles discharging from a rectangular hopper using distinct element method and comparison with experimental data (effects of time steps and material properties). Adv Powder Technol, 1995, 6: 259–269

18   Zou X Y, Wang Z L, Hao Q Z, et al. The distribution of velocity and energy of saltating sand grains in a wind tunnel. Geomorphology, 2001, 36: 155–165

19   Kang L Q, Guo L J, Gu Z M, et al. Wind tunnel experimental investigation of sand velocity in aeolian sand transport. Geomorphology, 2008, 97: 438–450

20   Dong Z B, Liu X P, Wang H T, et al. The flux profile of a blowing sand cloud: A wind tunnel investigation. Geomorphology, 2002, 49: 219–230